第 42 卷 第 10 期 焊 接 学 报 Vol. 42(10):08 − 13
2021 年 10 月 TRANSACTIONS OF THE CHINA WELDING INSTITUTION October 2021

铝合金爬坡 TIG 焊熔池失稳状态的视觉检测

洪宇翔[1], 杨明轩[1], 都东[2], 常保华[2], 肖宏[3]

(1. 中国计量大学, 浙江省智能制造质量大数据溯源与应用重点实验室, 杭州, 310018; 2. 清华大学, 先进成形制造教育部重点实验室, 北京, 100084; 3. 天津航天长征火箭制造有限公司, 天津, 300462)

摘要: 对焊接过程中的熔池状态进行视觉检测是实现焊缝质量在线监测的重要手段. 针对中厚板铝合金爬坡钨极氦弧焊过程易出现的熔池失稳和成形缺陷问题, 提出了一种基于熔池图像特征的钨极惰性气体保护焊 (TIG) 焊接状态监测方法. 基于构建的被动视觉传感系统, 实现强弧光干扰条件下清晰熔池图像的获取. 提出了一种基于 Otsu's 阈值分割和视觉显著性特征 (VSF) 的氦弧焊熔池图像处理算法, 用于提取熔池图像的形态特征, 并分析了所提取视觉特征与铝合金爬坡 TIG 焊过程稳定性的关系. 最后建立了支持向量机 (SVM) 模型实现熔池稳定性状态的在线识别. 结果表明, 相对于熔池轮廓几何特征, 熔池尾端熔融金属的形态特征能够更有效地反映出铝合金爬坡 TIG 焊过程中出现的熔池不稳定状态. 所建立的焊接状态分类模型在单一特征输入条件下, 最高准确率达到 95.94%. 所提出的实时检测方法为大型铝合金构件 TIG 焊缝成形缺陷的在线智能诊断与工艺优化提供了基础.

创新点: (1) 提出了一种基于 Otsu's 阈值分割和视觉显著性特征 (VSF) 的图像处理算法, 实现了氦弧焊中熔池尾端熔融状态区域特征的快速提取.

(2) 发现了位于熔池尾端局部轮廓平直度可以有效表征铝合金爬坡钨极氦弧焊过程中的不稳定状态.

(3) 建立了基于 SVM 的焊接状态分类模型, 在单一特征输入条件下, 最高准确率达到 95% 以上.

(4) 为实现大型铝合金构件 TIG 焊缝成形缺陷在线智能诊断和焊接工艺优化提供基础.

关键词: 爬坡 TIG 焊; 中厚板铝合金; 焊接过程检测; 视觉传感; 熔池特征

中图分类号: TG 409 **文献标识码:** A **doi:** 10.12073/j.hjxb.20201208001

0 序言

铝合金爬坡钨极惰性气体保护焊 (climbing-TIG) 是航空航天工业中重要的装备制造技术, 其中氦弧焊因具有更大的熔深, 能量分布更集中而应用在一些关键零部件的焊接中[1], 如运载火箭的贮箱封头焊接. 然而, 中厚板铝合金爬坡钨极氦弧焊技术在焊缝成形质量稳定性方面仍面临挑战, 尚缺乏系统的理论基础和有效的解决途径.

对焊接成形过程进行实时传感能够连续获取其瞬态过程信息, 可用于焊接质量评价与追溯, 并为指导焊接工艺优化提供依据. 焊接过程质量信息传感的手段多种多样, 国内外研究人员针对超声检测[2], 光谱分析[3-4], 可听声[5], 视觉传感[6-11] 等方式开展了大量的研究. 其中, 熔池区域的视觉传感技术由于其非接触, 信息量丰富而广受关注. 田纳西大学采用被动视觉系统提取能够表征三维熔池表面的视觉特征, 并基于此实现了熔池背面宽度的预测[6]. 江苏科技大学针对焊接图像存在噪声、对比度低、边缘模糊等问题, 提出了一种有效的焊接缺陷区域特征提取方法, 并成功用于孔隙、裂纹和焊接缺陷的大小的识别[7]. 五邑大学建立了一种基于 CNN 的视觉模型, 能够识别包括 V 形、曲线型等各种形态的焊缝[8]. 华中科技大学采用红外 CCD 在线采集熔池红外图像, 并基于改进的熔池特征提取算法成功实现了烧穿、未熔透等缺陷的在线识别[9]. 肖宏等人[10] 采用二值图像形态学算法获得了铝合金钨极氦弧焊中的熔池宽度特征尺寸. 清华大学通过视觉传感的方式采集铝合金 GTAW 中焊缝背面图像进而对焊接过程中的焊缝熔深进行监控[11].

目前基于视觉传感的焊接过程稳定性的研究大多是以平焊位置的钨极氩弧焊为试验对象, 关于

收稿日期: 2020 − 12 − 08

基金项目: 国家自然科学基金资助项目 (51605251); 国防基础科研计划 (JCKY2014203A001).

爬坡氦弧焊的成形质量在线检测方法鲜有报道. 文中针对中厚板铝合金爬坡氦弧焊，提出了一种基于熔池图像特征的实时监测方法，对比分析了熔池区域采集特征的有效性. 最后得出熔池尾端熔融金属的形态特征能够有效表征铝合金爬坡氦弧焊过程中出现的熔池不稳定状态.

1　试验系统及参数

试验系统主要包括焊接电源、工控机、氦气保护气体、焊枪、视觉传感器和图像采集系统. 其中视觉传感器成像装置采用瑞士 Photonfocus 公司生产的 CMOS 工业相机，滤光片 (660 nm + 10 nm) 前置于相机镜头前端. 工件材料为 9.5 mm 厚 2219 铝合金板，工件尺寸为 300 mm × 150 mm. 焊接试验为铝合金爬坡 TIG 焊，焊接工艺为钨极氦弧焊，焊接试验系统如图 1 所示，焊接工艺参数如表 1 所示. 焊接过程中采用视觉传感器从熔池后方连续采集熔池正面图像，如图 2 所示.

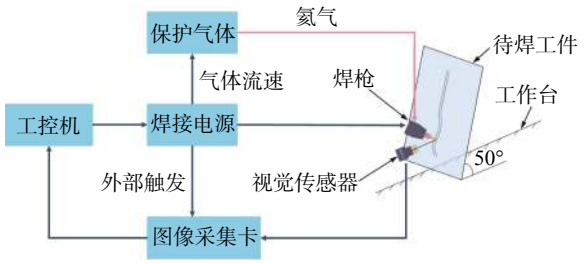

图 1　焊接试验系统示意图

Fig. 1　Schematic diagram of welding experiment system

表 1　焊接试验参数

Table 1　Welding experiment parameters

焊接速度 v_h/(mm·min^{-1})	氦气流量 q/(L·min^{-1})	焊接电流 I/A	焊接电压 U/V	钨极直径 d/mm
200	12	290 ~ 300	24.5	5.0

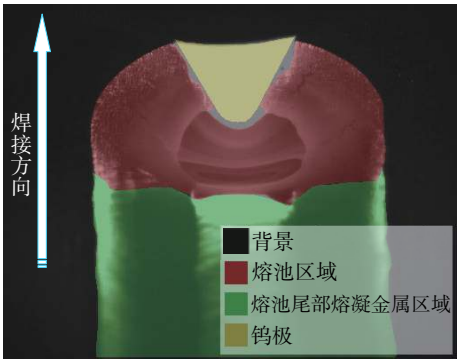

图 2　熔池图像分析

Fig. 2　Image analysis of welding pool

2　熔池特征量化与提取

2.1　熔池特征量化

从熔池区域共提取了 6 种特征，为了能更好的反应特征与焊接状态稳定性之间的关系，对采集的特征进行量化，详细信息如图 3 所示. 其中δ为熔池尾端局部轮廓的平直度，用于表征熔池尾端熔融金属的形态特征；W_o为熔池及其尾端区域联合的最大宽度；C_x, C_y为熔池质心，W_m, L_m分别为熔池的最大宽度和最大长度.

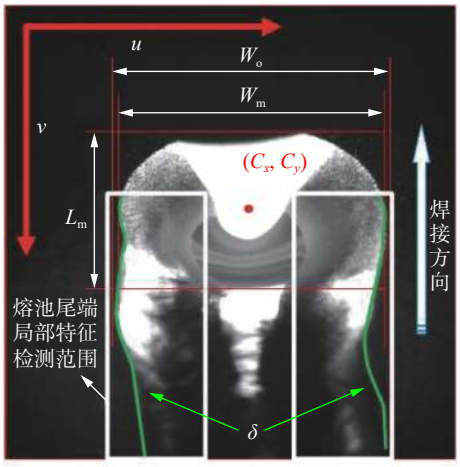

图 3　熔池特征参数定义

Fig. 3　Definition of molten pool characteristic parameters

结合铝合金爬坡氦弧焊的熔池图像特点，对熔池尾端熔融金属轮廓的平直度进行度量，熔池尾端局部轮廓由两部分组成，分别为左侧和右侧的轮廓，熔池尾端局部单侧轮廓平直度δ_i量化为

$$\delta_i = \sum_{n=1}^{N_i} \frac{|\Delta L_{in}|}{L_{in}}, i = l, r \tag{1}$$

式中：L_{in}为熔池尾端局部轮廓在 u 轴方向的像素坐标值；$|\Delta L_{in}|$为熔池尾端局部轮廓边界到L_{in}距离的绝对值；N_i为熔池尾端局部轮廓沿 v 轴方向的像素点总数；l表示熔池尾端局部轮廓沿 v 轴方向的左侧部分；r表示熔池尾端局部轮廓沿 v 轴方向的右侧部分；其中ΔL_i的计算为

$$\Delta L_{\mathrm{l}} = \sum_{i=1}^{N_{\mathrm{l}}} \left(L_{l_i} - \min_{(u,v)\in S_{\mathrm{l}}} u \right) \tag{2}$$

$$\Delta L_{\mathrm{r}} = \sum_{j=1}^{N_{\mathrm{r}}} \left(\max_{(u,v)\in S_{\mathrm{r}}} u - L_{r_j} \right) \tag{3}$$

式中：S_1为熔池尾端局部轮廓区域像素坐标值集合.

$$\delta = \alpha \cdot \delta_l + (1-\alpha)\cdot \delta_r,\ 0 \leqslant \alpha \leqslant 1 \tag{4}$$

式中：α为平直度因子，是用于衡量熔池尾端左右两侧局部轮廓的重要性. 其计算公式为

$$\alpha = \frac{\max L_{\mathrm{l}}}{\max L_{\mathrm{l}} + \max L_{\mathrm{r}}} \tag{5}$$

$$C_x = \frac{\sum_{i=1}^{n}\sum_{j=1}^{m} G(i,j)\cdot i}{\sum_{i=1}^{n}\sum_{j=1}^{m} G(i,j)} \tag{6}$$

$$C_y = \frac{\sum_{i=1}^{n}\sum_{j=1}^{m} G(i,j)\cdot j}{\sum_{i=1}^{n}\sum_{j=1}^{m} G(i,j)} \tag{7}$$

式中：$G(i,j)$表示像素在像素坐标系中(i,j)位置的灰度值.

$$W_{\mathrm{o}} = \max_{(u,v)\in S_1} u - \min_{(u,v)\in S_1} u \tag{8}$$

$$W_{\mathrm{m}} = \max_{(u,v)\in S_2} u - \min_{(u,v)\in S_2} u \tag{9}$$

$$L_{\mathrm{m}} = \max_{(u,v)\in S_2} v - \min_{(u,v)\in S_2} v \tag{10}$$

式中：S_2为熔池区域像素坐标值集合.

2.2 熔池特征提取算法

视觉注意机制是指通过算法模拟人的视觉特点来提取图像中的感兴趣区域，主要有自下向上和自上而下两种策略. 经典模型有 Itti-Koch-Niebur 模型、Itti 模型、GBVS 模型等. 自下而上的注意机制主要利用图像的颜色、亮度、边缘等特征判断目标区域与周围像素的差异来计算图像的显著性区域；自上而下的注意机制主要是通过对图像的特定特征来计算图像区域的显著性. 文中主要采用 Sebastian Montabone 在 2010 年提出的基于视觉显著性特征 (VSF) 的显着性检测方法.

熔池特征提取算法主要分为两个步骤，如图 4 所示. 首先是基于 Otsu's 阈值分割的自适应感兴趣区域 (ROI) 提取，其中灰度切割和 Otsu's 阈值分割用于提取熔池的大致轮廓，形态学开运算用于对处理后的二值图像去噪. 最后基于提取的熔池大致轮廓能够确定熔池区域的 ROI. 通过提取 ROI 能够降低采集的原始图像周围飞溅等因素的干扰. 其次是基于 VSF 显著性检测的精确熔池轮廓提取. 通过自适应直方图均衡化和基于 VSF 的显著性检测方法能够显著增强熔池的外轮廓，之后通过顶帽操作来滤除熔池内其它因素的干扰，从而提取出精确的熔池轮廓.

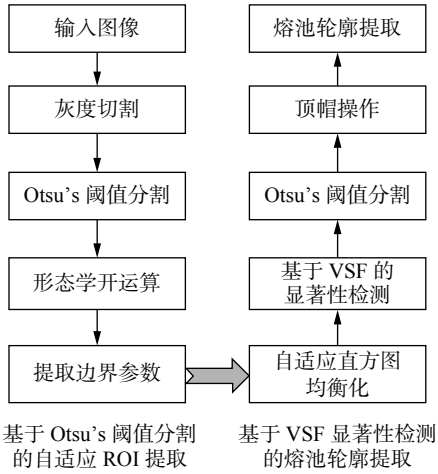

图 4 基于显著性检测的熔池特征提取流程图

Fig. 4 Flow chart of feature extraction of molten pool based on saliency detection

3 熔池状态预测模型

支持向量机由于优异的分类性能，已经成为应用最为广泛的机器学习分类算法. 其主要是将输入的欧式空间的数据映射为特征空间的特征向量，然后在特征空间中进行分类. 其间隔最大化的学习策略能够最大限度的保证模型的分类性能，提高模型的鲁棒性. 文中主要采用线性支持向量机进行二分类验证所提取特征的有效性，其算法如下. 设输入

$$x_i \in \chi = R^n, y_i \in \gamma = \{+1,-1\}, i = 1,2,\cdots,N$$

式中：x_i为第i个特征向量；y_i为x_i的标签. 约束条件为

$$y_i(\omega \cdot x_i + b) \geqslant 1 - \xi_i, \xi_i \geqslant 0 \tag{11}$$

式中：ξ_i为松弛变量. 构造并求解凸二次规划问题，即

$$\min_{\omega,b,\xi} \frac{1}{2}\|\omega\|^2 + C\sum_{i=1}^{N}\xi_i \tag{12}$$

$$\mathrm{s.t.} y_i(\omega \cdot x_i + b) \geqslant 1 - \xi_i, i = 1,2,\cdots,N \tag{13}$$

$$\xi_i \geqslant 0, i = 1,2,\cdots,N \tag{14}$$

通过求解软间隔最大化问题得到的分类超平面为

$$\omega^* \cdot x + b^* = 0 \tag{15}$$

得到相应的分类决策函数为

$$f(x) = \mathrm{sign}(\omega^* \cdot x + b^*) \tag{16}$$

4　试验结果与分析

4.1　熔池图像处理与特征提取

利用提出的特征提取算法对熔池失稳状态和稳定状态采集的熔池图像序列进行处理，典型缺陷及成形良好的熔池图像如图 5 所示．每隔 80 ms 采集一帧图像，连续采集 6 帧具有代表性的图像，从上到下的 1 ~ 5 帧为失稳状态阶段的图像，第 6 帧为稳定状态阶段采集的图像，然后对图像进行处理，图 5 展示了部分关键的处理步骤，从左到右分别为先进行直方图均衡化和显著性检测的组合处

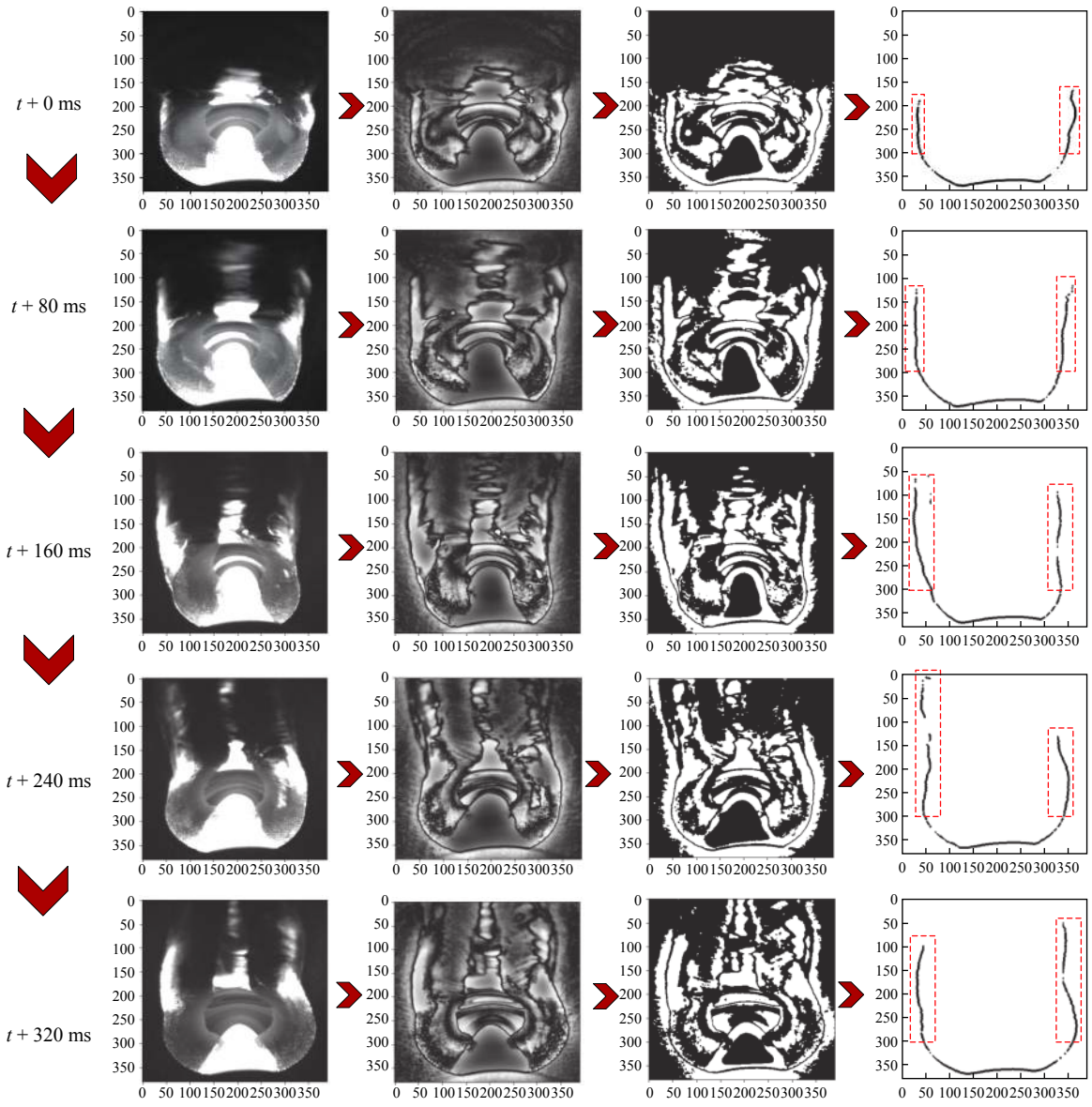

(a) 熔池失稳状态阶段

(b) 熔池稳定状态阶段

图 5　熔池尾端局部轮廓特征提取

Fig. 5　Feature extraction of local profile at the end of molten pool. (a) instabillty stage of molten pool; (b) stabillty stage of molten pool

理得到第二列轮廓清晰的熔池图像，进行 Otsu's 阈值分割得到第三列二值化图像，最后利用形态学处理中的顶帽操作得到第四列精确的熔池轮廓图像. 从图 5 可以得出，当焊接过程中出现失稳状态时会产生如咬边、熔池外翻、蛇形焊道等成形不良缺陷，对应熔池图像的局部轮廓会产生不规则的变化. 熔池失稳状态阶段采集的 1 ~ 5 帧图像的第四列熔池轮廓整体呈现坡形弯曲、S 形弯曲、M 形弯曲等，轮廓长度变化也不一致，呈现一边长一边短、两边短、两边长等，且宽度变化不一致. 而焊接过程稳定时，熔池尾端熔融金属形态稳定，如稳定状态阶段采集的第 6 帧图像，形成的焊缝纹理均匀，成形质量较好，对应的熔池局部轮廓相对较为平直，且长度和宽度均匀. 因此可以得出，熔池尾端局部轮廓形态在稳定阶段与失稳阶段有明显不同，熔池尾端局部轮廓的平直度的动态变化能够有效反映出焊接过程中的失稳状态，通过度量该特征能够对焊接过程的稳定性进行检测.

4.2 基于 SVM 的熔池状态预测

在铝合金爬坡 TIG 焊中，受熔池中熔融金属重力的影响，在爬坡的过程中熔池表面张力发生波动，受力平衡被打破，从而影响焊接过程中熔池的稳定性. 焊接试验将 9.5 mm 厚的 2219 铝合金板倾斜 50°，焊枪垂直工件向上移动，采集的焊缝实物图如图 6 所示. 将焊缝状态分为了两类，其中 I 类表示熔池失稳状态阶段，II 类表示熔池稳定状态阶段. 最后通过熔池状态预测模型识别焊接状态，总样本为 6 000 帧熔池图像序列，其中 4 020 帧用于模型训练，1 980 帧用于测试模型的准确率.

熔池区域提取的特征结果曲线如图 6 所示，从图中可以看出，δ特征前半部分曲线对应熔池失稳状态部分，其值普遍偏高且波动较大，且值越高熔池越不稳定，而后半段对应熔池稳定阶段的曲线波动较小，曲线整体比较平缓，该特征能够有效的表征焊接过程中的失稳状态. 熔池宽度W_m、熔池长度L_m、熔池质心C_x特征在熔池失稳阶段曲线波动无规律，且曲线波动幅度较小. 熔池质心C_y、熔池区域和熔池尾端局部轮廓区域的联合最大宽度W_o特征曲线则在整个焊接过程都比较平稳，对焊接过程中的熔池失稳状态并不敏感. 因此，经分析可以得出，熔池尾端局部轮廓平直度特征δ能够有效反映出铝合金爬坡氦弧焊过程中的失稳状态，其余特征则对焊接过程中的失稳状态和稳定状态的区分并不敏感.

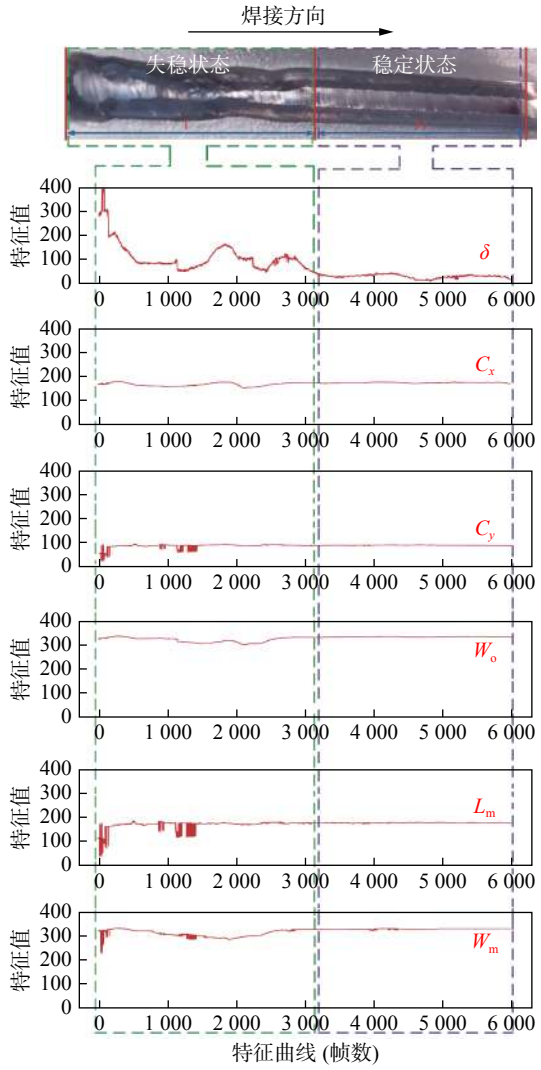

图 6 熔池特征参数与对应的焊接状态

Fig. 6 Characteristic parameters of the molten pool and the corresponding welding state

将采集的 6 种熔池特征分别单独输入到熔池状态预测模型中，得到的结果如表 2 所示，从表中可以

表 2 SVM 测试结果

Table 2 SVM test results

编号	特征名称	F1分数		准确率	
		训练集	测试集	训练集	测试集
1	δ	96.00%	95.98%	94.70%	95.94%
2	W_o	84.00%	86.51%	83.40%	86.38%
3	C_x	79.00%	76.16%	75.40%	76.09%
4	C_y	73.00%	48.95%	61.90%	62.32%
5	W_m	83.00%	86.96%	81.90%	86.81%
6	L_m	80.00%	77.76%	74.70%	77.54%

得出, 熔池尾端局部轮廓平直度特征δ在测试集上的分类精度最高, 达到了 95.94%. 而其余特征的准确率较差.

5　结论

(1) 提出了一种基于 Otsu's 阈值分割和 VSF 显著性检测的氦弧焊熔池图像处理算法, 实现了熔池尾端局部轮廓平直度、熔池长度, 熔池宽度、熔池质心、焊缝最大宽度的快速提取. 每帧处理时间小于 10 ms, 满足焊接状态监测的实时性需求.

(2) 熔池尾端局部轮廓平直度特征能够有效表征熔池尾端熔融金属的形态变化. 相对于熔池轮廓几何特征, 该特征能够更有效地反映出铝合金爬坡钨极氦弧焊过程中出现的熔池不稳定状态.

(3) 建立了基于 SVM 的焊接状态分类模型, 在单一特征输入条件下, 最高准确率达到 95.94%.

(4) 实现了铝合金爬坡 TIG 焊动态熔池行为的描述和失稳状态的实时监测, 为实现焊缝成形缺陷的在线智能诊断和焊接工艺优化提供了基础.

参考文献

[1] 赵红星, 王国庆, 杨春利, 等. 氦弧与氩弧电弧特性对比研究 [J]. 机械工程学报, 2018, 54(8): 137 − 143.
Zhao Hongxing, Wang Guoqing, Yang Chunli, *et al*. Comparative research of helium and argon arc characters[J]. Journal of Mechanical Engineering, 2018, 54(8): 137 − 143.

[2] Wang Y J, Yu C, Lu H, *et al*. Research status and future perspectives on ultrasonic arc welding technique[J]. Journal of Manufacturing Processes, 2020, 58: 936 − 954.

[3] 张志芬, 张林杰, 杨哲, 等. 航空航天用铝合金机器人焊接内部气孔缺陷在线检测 [J]. 航空制造技术, 2019, 62(Z2): 14 − 24.
Zhang Zhifen, Zhang Linjie, Yang Zhe, *et al*. On-line inner porosity defect detection of aluminum alloy robotic welding for aerospace[J]. Aerospace Manufacturing Technology, 2019, 62(Z2): 14 − 24.

[4] Huang Y M, Yuan Y X, Yang L J, *et al*. A study on porosity in gas tungsten arc welded aluminum alloys using spectral analysis[J]. Journal of Manufacturing Processes, 2020, 57: 334 − 343.

[5] Zhang Z F, Wen G R, Chen S B. Audible sound-based intelligent evaluation for aluminum alloy in robotic pulsed GTAW: mechanism, feature selection, and defect detection[J]. IEEE Transactions on Industrial Informatics, 2018, 14(7): 2973 − 2983.

[6] Chen Z Y, Chen J, Feng Z L. Welding penetration prediction with passive vision system[J]. Journal of Manufacturing Processes, 2018, 36: 224 − 230.

[7] Qi Jiyang, Li Jinyan. Feature extraction of welding defect based on machine vision[J]. China Welding, 2019, 28(1): 56 − 62.

[8] 李鹤喜, 韩新乐, 方灶军. 一种基于 CNN 深度学习的焊接机器人视觉模型 [J]. 焊接学报, 2019, 40(2): 154 − 160.
Li Hexi, Han Xinle, Fang Zaojun. A visual model of welding robot based on CNN deep learning[J]. Transactions of the China Welding Institution, 2019, 40(2): 154 − 160.

[9] 夏卫生, 龚福建, 杨荣国, 等. 基于红外视觉的熔化极气体保护焊外观缺陷识别 [J]. 焊接学报, 2020, 41(3): 69 − 73.
Xia Weisheng, Gong Fujian, Yang Rongguo, *et al*. Apparent defect recognition of gas metal arc welding based on infrared vision[J]. Transactions of the China Welding Institution, 2020, 41(3): 69 − 73.

[10] 肖宏, 宋建岭, 常保华, 等. 基于形态学算法的 2219 铝合金钨极氦弧焊熔池图像特征提取 [J]. 宇航材料工艺, 2019, 49(1): 78 − 81.
Xiao Hong, Song Jianling, Chang Baohua, *et al*. Image feature extraction of helium gas tungsten arc welding pool of 2219 aluminum alloy based on morphological algorithm[J]. Aerospace Materials & Technology, 2019, 49(1): 78 − 81.

[11] Peng G D, Gao Y J, Tian Z J, *et al*. Penetration control of GTAW process for aluminum alloy using vision sensing[J]. Journal of Physics: Conference Series, 2019, 1303: 012139.

第一作者: 洪宇翔, 博士, 特聘副教授;主要从事机器人与智能化焊接方面的科研和教学工作; Email: hongyuxiang@cjlu.edu.cn.

通信作者: 都东, 教授; Email: dudong@tsinghua.edu.cn.

（编辑:　郑红）

MAIN TOPICS, ABSTRACTS & KEY WORDS

Research on the RF performance simulation of ultra-fine wire bonding of RF devices WANG Shang[1], MA Jingxuan[1], YANG Dongsheng[1,2], XU Jiahui[1], HANG Chunjin[1], TIAN Yanhong[1] (1. State Key Laboratory of Advanced Welding and Joining, Harbin Institute of Technology, Harbin, 150001, China; 2. Guobo Electronics Co., Ltd., Nanjing, 211111, China). pp 1-7

Abstract: With the continuous improvement of radar performance indicators and the continuous compression of the volume, the T/R (transmitter and receiver) component as one of its key components is also continuously developing in the direction of miniaturization and high density. Ultra-high-density wire bonding technology is adopted to realize high-density RF device packaging form. However, it will cause the reliability of bonding solder joints to decrease, and the circuit RF performance is poor. Aiming at the problem of the degradation of radio frequency performance caused by the small bond size, this paper used HFSS software to explore the influence of the change in the gold strip's size on the circuit radio frequency performance. And ANSYS Q3D and ADS software were used to match the impedance of the ultra-fine wire bonding circuit. The results show that for gold wire and gold ribbon, inserting the microstrip double-stub matching structure can significantly improve the radio frequency performance of the circuit. For type 1 structure, the transmission power of S21 and S12 can reach −0.049 dB. For type 2 Structure, the transmission power of S21 and S12 can reach -7.245×10^{-5} dB, indicating that the signal transmission under the type 2 structure is almost lossless. This result can lay a theoretical foundation for the application of ultra-fine wire bonding technology in radio frequency circuits.

Highlights: (1) The model containing the microstrip transmission line is established in the electromagnetic field simulation software ANSYS HFSS. The span, arch height, cross-section size, number of gold wires and other parameters of the bonding alloy wire are changed, the insertion loss and return loss under different parameters are calculated, and the relationship between the RF performance of the gold wire bonding and the bonding structure parameters is found.

(2) The equivalent circuit model of the transmission line is established in the circuit simulation software ADS. Microstrip single-branch stub and microstrip double-branch stub structures are used to match the impedance of the mismatch circuit, and solutions that can reduce signal loss have been successfully discovered.

Key words: ultra-fine wire bonding; RF performance; impedance matching

Unstable state vision detection of molten pool during aluminum alloy climbing-TIG welding HONG Yuxiang[1], YANG Mingxuan[1], DU Dong[2], CHANG Baohua[2], XIAO Hong[3] (1. Key Laboratory of Intelligent Manufacturing Quality Big Data Tracing and Analysis of Zhejiang Province, China Jiliang University, Hangzhou, 310018, China; 2. Key Laboratory for Advanced Materials Processing Technology, Ministry of Education, Tsinghua University, Beijing, 100084, China; 3. Tianjin Aerospace Long March Rocket Manufacturing Co. Ltd., Tianjin, 300462, China). pp 8-13

Abstract: Visual detection of the state of the molten pool during the welding process is an important means to realize the online monitoring of weld quality. Aiming at the problems of molten pool unstable state and forming defects that are likely to occur during the climbing tungsten helium arc welding process of medium and thick aluminum alloys, this paper proposes a Tungsten Inert Gas Welding(TIG) welding status monitoring method based on the image characteristics of the molten pool. Based on the constructed passive vision sensor system, the acquisition of clear images of the molten pool under the interference of strong arc light is realized. A helium arc welding based on Otsu's threshold segmentation and visual saliency features(VSF) is proposed. The image processing algorithm of the molten pool is used to extract the morphological features of the molten pool, and the relationship between the extracted visual features and the stability of the aluminum alloy climbing-TIG welding process is analyzed. Finally, a support vector machine (SVM) model is established to identify the welding state. The experimental results show that, compared with the geometric characteristics of the molten pool contour, the morphological characteristics of the molten

metal at the end of the molten pool can more effectively reflect the unstable state of the molten pool during the aluminum alloy climbing-TIG welding process. The established welding state classification model has a maximum accuracy of 95.94% under the condition of a single feature input. The proposed real-time detection method provides a basis for online intelligent diagnosis and process optimization of TIG weld forming defects of large aluminum alloy components.

Highlights: (1) An image processing algorithm based on Otsu's threshold segmentation and visual saliency features (VSF) is proposed to quickly extract the features of the melt state region at the molten pool tail during helium tungsten arc welding.

(2) It was found that feature δ located at the tail of the molten pool can effectively characterize the unstable state of the aluminum alloy during climbing helium tungsten-arc welding.

(3) A welding state classification model based on SVM was established, and the highest accuracy was more than 95% under the condition of a single feature input.

(4) This research provides a basis for the online monitoring of aluminum alloy defects during climbing TIG welding.

Key words: climbing-TIG welding; medium and thick plate aluminum alloy; welding process detection; visual sensing; molten pool features

Influences of preheating temperatures on the microstructures and mechanical properties of GTA additive manufactured TiAl based alloy CAI Xiaoyu, DONG Bolun, YIN Xianlai, LIN Sanbao, FAN Chenglei (State Key Laboratory of Advanced Welding and Joining, Harbin Institute of Technology, Harbin, 150001, China). pp 14-21

Abstract: High-temperature structural material TiAl based alloy has poor machinability. It is challenging to fabricate complex structures. And the processing cost is relatively high. GTA arc additive manufacturing is a promising technology to synthesis TiAl based alloy in situ with increased flexibility and low cost. However, crack control is still essential during fabrication. Preheating is effective in avoiding cracking during additive manufacturing. In this work, the Ti6Al4V and ER1100 wires are used as feedstock to fabricate TiAl based alloy in situ with an aluminum content of 50 at%. Preheating temperatures of 200, 300, 450 ℃ are used to investigate the influences on the microstructures and mechanical properties of the fabricated specimen. Results show that, with the preheating temperature increasing, more bulk γ phases precipitate on the boundaries of γ/α_2 lamellar clusters in the top and middle region of the specimen, while the influences on the microstructures at the bottom are not significant. The proportion of α_2 decreases with the preheating temperature, leading to a diminishing hardness. At the same time, the percentage of bulk-like γ phases increases, which results in the promotion of compressive properties. When the preheating temperature is set at 450 ℃, the fabricated specimen shows the highest compressive strength and compression ratio.

Highlights: (1) V containing TiAl based alloy is successfully fabricated in situ by feeding Ti6Al4V and ER1100 wires simultaneously.

(2) Influences of preheating temperatures on the microstructures and mechanical properties of additively manufactured TiAl based alloy are illuminated.

Key words: wire arc additive manufacturing; TiAl based alloy; preheating temperature; microstructures; mechanical properties

Effect of strain aging on fracture toughness of welded joints of high-strain pipeline steel GAO Shanshan[1], DI Xinjie[1], LI Chengning[1], JIANG Yuanbo[1], LI Weiwei[2], JI Lingkang[2] (1. Tianjin University, Tianjin, 300350, China; 2. CNPC Tubular Goods Research Institute, Xi'an, 710077, China). pp 22-28

Abstract: In order to explore the effect of strain aging on welded joints of high strain pipeline steel, the microstructure and mechanical properties of welded joints of high strain pipeline steel before/after strain aging were studied. The mechanical properties of welded joints before/after strain aging were investigated by hardness test, fracture toughness test and digital image correlation (DIC) strain test. The microstructure and substructure characteristics of welded joints were analyzed based on optical microscope (OM), scanning electron microscope (SEM), electron back-scattered diffraction (EBSD) technology and X-ray diffraction technology. The results indicated that the microstructure of welded joint does not change obviously after strain aging, but the inside microdefects increase. Meanwhile, the fracture toughness of welded joints decreases, and the decrease amplitude increases with the pre-strain degree. It was found that the increase of dislocation density, strain concentration as well as the geometrically necessary dislocation (GND) density are key factors leading to the decrease of plastic deformability and the deterioration of fracture toughness of welded joints.

Highlights: (1) The microstructure evolution and mechanic-